Supplementary Materials for

Measuring and Manipulating Defect-induced Micro-electronic Fields at Metal-Support Interface

Yi Wei *et al.*

*Corresponding author. Email:
jldu@pku.edu.cn (Jinlong Du), sunqiang@pku.edu.cn (Qiang Sun), efu@pku.edu.cn (Engang Fu)

This PDF file includes:

Supplementary Text
Figs. S1 to S24
Tables S1 to S8
References

Supplementary Text

Calculation of the nuclear and electronic energy loss induced by heavy ion irradiation

The heavy ion irradiation induced damage on the target materials is mainly caused by electron energy loss and nuclear energy loss as is described in formula (1). Typically, the electron energy loss induced material damage performs as the break and reconstruction of the chemical bond, while the nuclear energy loss of the incident ions tends to lead to the atom shift and displacement.

$$-\frac{dE}{dx} = \left(-\frac{dE}{dx}\right)_{electron} + \left(-\frac{dE}{dx}\right)_{nuclear} \quad (1)$$

According to the Bethe-Bloch formula (2), the electron stopping power is proportional to $\frac{1}{v^2}$ of the incident ions at low energy and proportional to lnv^2 at high energy.

$$(-\frac{dE}{dx})_{electron} = \frac{4\pi k^2 e^4 N_A}{m_e c^2}\frac{z^2}{\beta^2}\frac{\rho Z}{A}\left[\frac{1}{2}ln\left(\frac{2m_e c^2\beta^2\gamma^2 T_{max}}{I^2}\right) - \beta^2 - \delta(\beta) - \frac{c}{Z}\right] \quad (2)$$

Where z refers to the atom number of incident ions, Z, ρ, A is the atom number, density, mass number of target materials. T_{max} is the max kinematic energy transferred from particle onto target electrons. $\frac{c}{Z}$ is the shell corrections. $\delta(\beta)$ is the density correction due to the polarization. Hence there's extremums of electron energy loss. Based on the Monte Carlo simulation, we employ SRIM to calculate the two different energy loss of 0.5-6 MeV C^+ separately. As for the electron energy loss shown in Figure S2, the value almost reaches the peak at approximate 3 MeV. It illustrates that the 3 MeV C^+ will cause 160 MeV energy loss when it moves 1 mm. Correspondingly, the nuclear energy loss could be calculated as follows formula (3):

$$(-\frac{dE}{dx})_{nuclear} = \frac{4\pi k^2 e^4 N_A}{m_e c^2}\frac{z^2}{\beta^2}\frac{\rho Z}{A}\left[ln\left(\frac{2m_e v^2}{I}\right) - 1.2329\right] \quad (3)$$

The as calculated nuclear energy loss of the 3MeV C^+ is less than 0.5 MeV mm^{-1}. It suggests that electron energy loss takes the position in the process of self-ion irradiation. Therefore, in this work the heavy ion irradiation mainly caused the C-C bond fracture and reconstruction, arising from the cascade collision of the incident C^+ with CNTs. The electron energy loss process mainly consists of the ionization and excitation of the target C atoms on CNTs. Once the outside electrons of target C atoms are excited, the ionized electron-deficient C atoms tend to form new chemical bond with electron-rich C atoms, resulting in the formation of the topological defects (including pentagon, hexagon, heptagon and octagon.etc) configuration on CNTs without forming the large vacancies or complex defects (single atom, heteroatom doping.etc). This is consistent with the Raman spectrum of the irradiated CNTs, which shows little change of the I_D/I_G ratio, suggesting the low density of the vacancies and nonexistence of heteroatoms.

Four-Dimensional Scanning Transmission Electron Microscopy

Dataset collection: The scanning diffraction datasets are collected by high-speed pixelated electron detector (Gatan OneView) working at the accelerating voltage of 60 kV. The carbon liked materials consisting of light elements is hard to analysis through the complete diffraction information collected by the common electron microscope operated with accelerating voltage of 200-300 kV.

Analysis of the reconstructed datasets: In the 4D datasets collection systems, the negative nature of the electrons promised the deflection of the transmitted electrons when an electron probe propagated through the electric field. In this collection experiments, the momentum changes of the electrons arising from the electric field will lead to the probe shifting in the diffraction plane, which is in a negatively proportional way to the electric field. Therefore, we could calculate the electron momentum change based the detected diffraction intensity redistribution by means of the pixelated electron detector acquiring each diffraction pattern in its entirety.

Thickness estimation of the model material: The thickness of the support carbon material and loaded Pt NP is measured through the HAADF and HRTEM data, and confirmed by analysis of the reconstructed BF and HAADF datasets. The related structure was revealed by diffraction pattern and reconstructed BF and HAADF imaged using py4DSTEM library. The reconstructed images were then Gaussian filtered to reduce the noise in the collected datasets through computer vision library. The estimated thickness based on the experimental HAADF and HRTEM datasets was then compared to the ratio from the reconstructed data, and the known width-to-height ratio of ~2.8 for the loaded Pt particles on the MWCNTs substrates was employed to estimate the thickness of the support as roughly x nm for the sample in Figure 3 and 4. The outer diameter and thickness at different distance to the axis along the radius especially the metal-support interface sites were estimated to be x from the constructed data and compared to the experimental ones.

Multipole expansion of the local charge distribution and the polarization of the atoms

The measurement of the local charge distribution on the model system is based on the MWCNTs and platinum NPs, which contain hundreds of carbon and platinum atoms. The nanometer scale resolution may not show the atomic polarization of the model system directly. Therefore, the correlations between the atomic results presented by DFT calculations and the nanometer scale reconstruction of the local charge distribution needs to be discussed in detail. Typically, for any local charge distribution of a model system in classical electrodynamics, the electric potential at position P with the distance r to the origin point can be described as:

$$V(r) = \frac{1}{4\pi\varepsilon_0}\int \frac{1}{\varkappa}\rho(r')d\tau' \quad (4)$$

Where $\rho(r')$ is the area charge density of the system, r' is the distance of the origin point to the point charge source. ε_0 refers to the vacuum permittivity, $\varkappa$ is the distance of P to the point charge source.

According to the multipole expansion method, the electric potential of local charge potential could be written as using Legendre polynomials:

$$V(r) = \frac{1}{4\pi\varepsilon_0}\sum_{n=0}^{\infty}\frac{1}{r^{n+1}}\int (r')^n P_n(cos\theta')\rho(r')d\tau' \quad (5)$$

Where $P_n(cos\theta')$ is Legendre Polynomials, θ' is the angle of r' and r. For more details, the electric potential is:

$$V(r) = \frac{1}{4\pi\varepsilon_0}\left[\frac{1}{r}\int \rho(r')d\tau' + \frac{1}{r^2}\int r'cos\theta'\rho(r')d\tau' + \frac{1}{r^3}\int (r')^2\left(\frac{3}{2}cos^2\theta' - \frac{1}{2}\right)\rho(r')d\tau' + \cdots\right] \quad (6)$$

It is clear that in the multipole expansion results, the electric potential mainly consists of the single pole, dipole term, quadruple term, eight-pole term and more higher pole terms. While the total charge of the system is approximately to be zero, the main contribution item of the system should be ascribed to the dipole term (neglecting the high order terms). In this system, the topological defects on the CNTs break up the valence balance of the CNT's intrinsic hexagon configuration, resulting in the atomic polarization of the carbon atom at the defective sites. This polarization eventually causes the formation of micro-electric field on interface the Pt-CNTs. Therefore, the electric potential of the dipole term can be described as:

$$V_{dipole}(r) = \frac{1}{4\pi\varepsilon_0}\frac{1}{r^2}\int r'cos\theta'\rho(r')d\tau' = \frac{1}{4\pi\varepsilon_0}\frac{p\cdot\hat{r}}{r^2} \quad (7)$$

Accordingly, the electric field of the dipole term is:

$$E_{dipole}(r,\theta) = \frac{p}{4\pi\varepsilon_0 r^3}\left(2cos\theta\hat{r} + sin\theta\hat{\theta}\right) \quad (8)$$

Electrochemical measurements

Catalyst ink preparation: The material Pt-Pristine-CNT, Pt-1E13-CNT, Pt-1E14-CNT, Pt-1E15-CNT were labelled as Sample #1, #2, #3, #4 before electrochemical test. Then 1 mg of the as-obtained sample material was dispersed in a mixture solution of ultrapure water, isopropanol and Nafion 117 solution (volume ratio=1:1:0.1) by sonication for 1 h to get the catalyst ink.

Electrochemical test system: Electrochemical activity measurements for HER were carried out based on the conventional three electrode electrochemical cell through CHI 760E with Ag/AgCl (saturated KCl solution) and graphite rod as the reference and counter electrode, respectively, and a glassy carbon (GC) electrode with a disk diameter of 5 mm covered by the catalyst ink as working electrode. 10 μl of the ink was deposited on the GC electrode, and the metal loading of every test was controlled to be no more than 10 μg cm^{-2}.

Electrochemical test conditions: For electrochemical assessments, fast cyclic voltammograms (CVs, 0.5 V s^{-1}, -0.25-0.8 V, in 0.1 M N_2-saturated $HClO_4$ solution) were conducted to activate the catalysts until stable states were obtained. Then the slow CVs at 0.005 V s^{-1} from -0.05 to 1.25 V were recorded. HER polarization curves were recorded in 0.1 M N_2-saturated $HClO_4$ solution at 0.005 V s^{-1} and a rotating speed of 1600 rpm. All HER curves were iR-recorrected before applying the

Calculation of performance indicators: All recorded potentials were calibrated to the RHE according to the Equation (9):

$$E_{RHE} = E_{Ag/AgCl} + 0.0592\cdot pH + 0.197 \quad (9)$$

Where E_{RHE} and $E_{Ag/AgCl}$ are the potentials relevant to RHE and Ag/AgCl, respectively.

Tafel slopes were calculated on the basis of the LSV profiles according to the Tafel Equation (10):

$$\eta = b \cdot \log\left(\frac{j}{j_0}\right) (10)$$

Where η is the overpotential ($\eta = |E_{RHE}|$), b is the Tafel slope, j is the recorded current density, and j_0 is the exchange current density.

The turnover frequency (TOF) could be calculated as Equation (11):

$$TOF = \frac{N_{H_2/S}}{N_{A/S}} (11)$$

Where $N_{H_2/S}$ is the H_2 molecule number per unit area, and $N_{A/S}$ is the active site number per unit area.

$$N_{\frac{H_2}{S}} = |J(mA\ cm^{-2})| \cdot \frac{1\ (C\ s^{-1})}{1000\ (mA)} \cdot \frac{1\ (mol\ e^{-1})}{96485.3\ (C)} \cdot \frac{1\ (mol)}{2\ (mol\ e^{-1}\ )} \cdot \frac{N_A}{1\ mol\ H_2} = 3.12 \times 10^{15}|J|(s^{-1}cm^{-2}) (12)$$

$$N_{A/S} = N_{Pt/S} = \frac{\frac{M}{S}(g\ cm^{-2}) \cdot Pt\ wt\%}{M_A} \cdot N_A (13)$$

Where J is the recorded current density, N_A is the Avogadro constant ($N_A = 6.022 \times 10^{23}$), $\frac{M}{S}$ is the catalyst loading per unit area, and M_A is the atomic mass of platinum.

The mass activity (MA) could be calculated from the current density that normalized by the mass loading at the certain overpotential as descripted by the Equation (14):

$$MA = \frac{J \cdot A_{disk}}{m_{atomic\ Pt}} (14)$$

Where A_{disk} is the area of the GC electrode, J is the current density, and $m_{atomic\ Pt}$ refers to the mass of atomic Pt on the electrode.

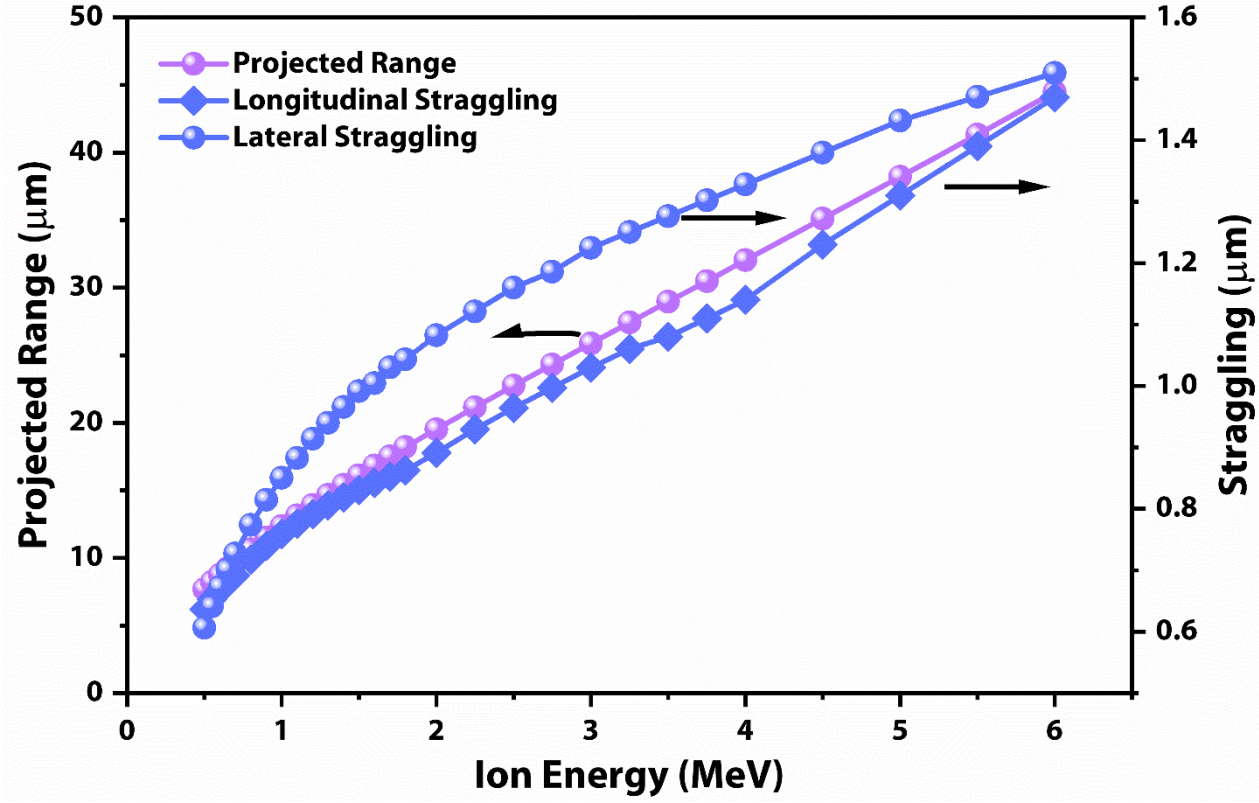

Figure.S1 The relationship between the energy and range of the incident C^+ ions

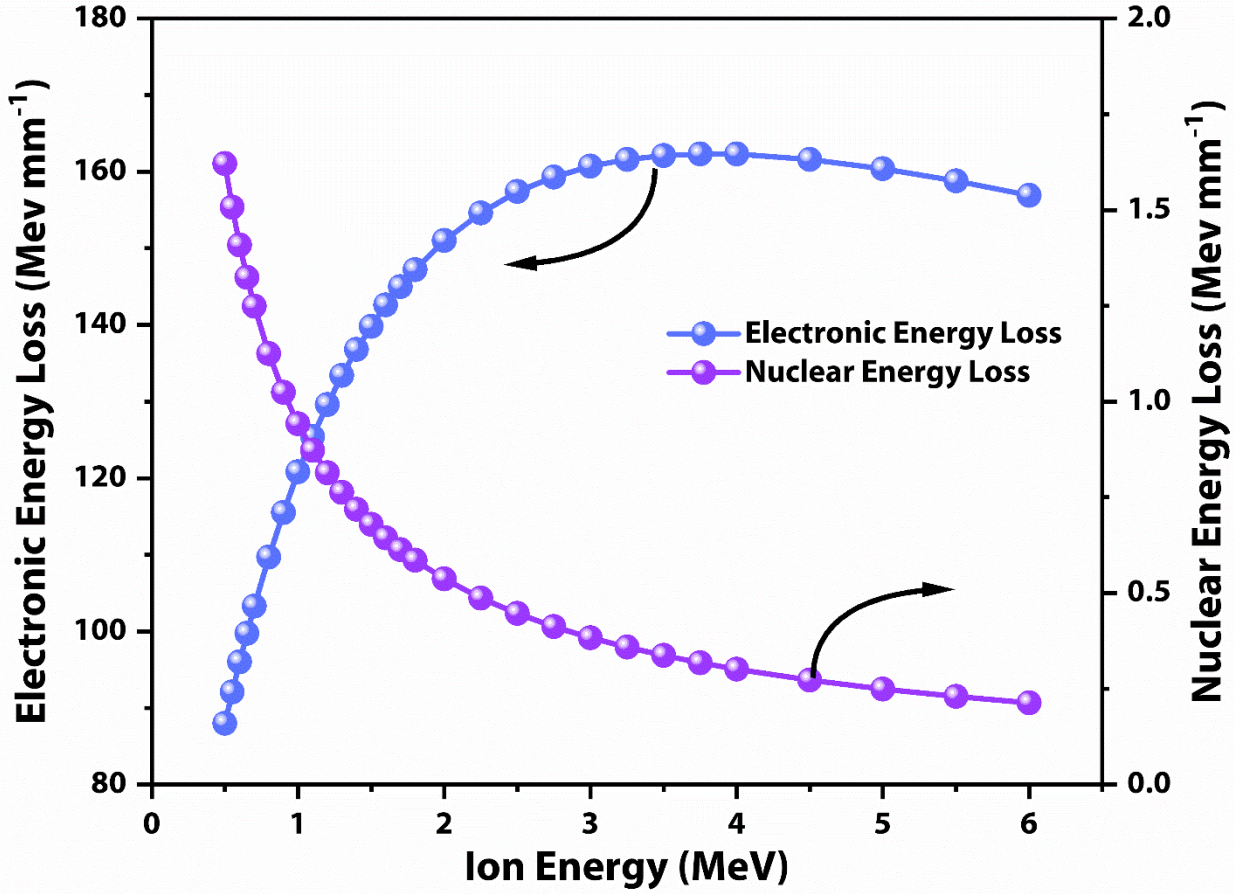

Figure.S2 The calculation of electronic and nuclear energy loss of C^+ with different energy projected in the MWCNTs

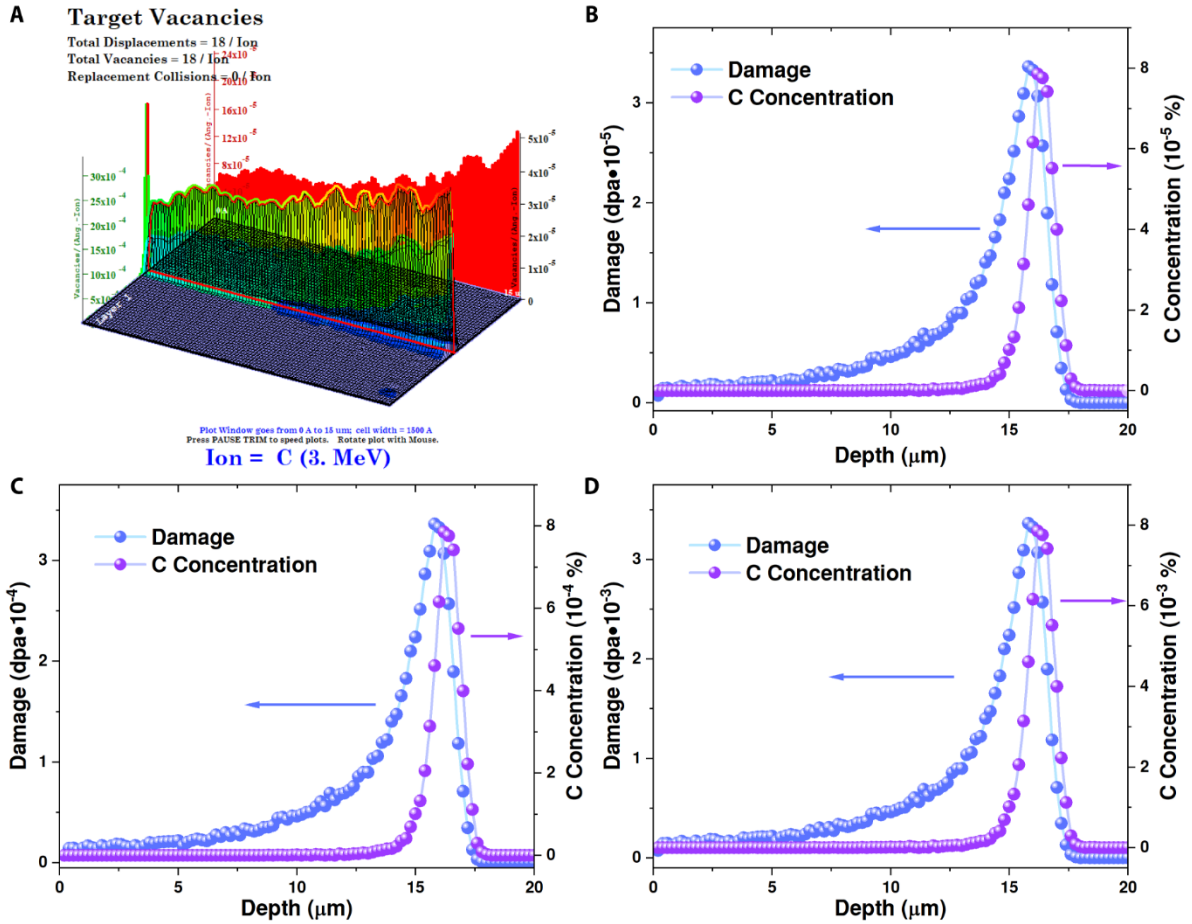

Figure.S3 The depth profile of radiation damage (in units of displacements per atom (DPA))

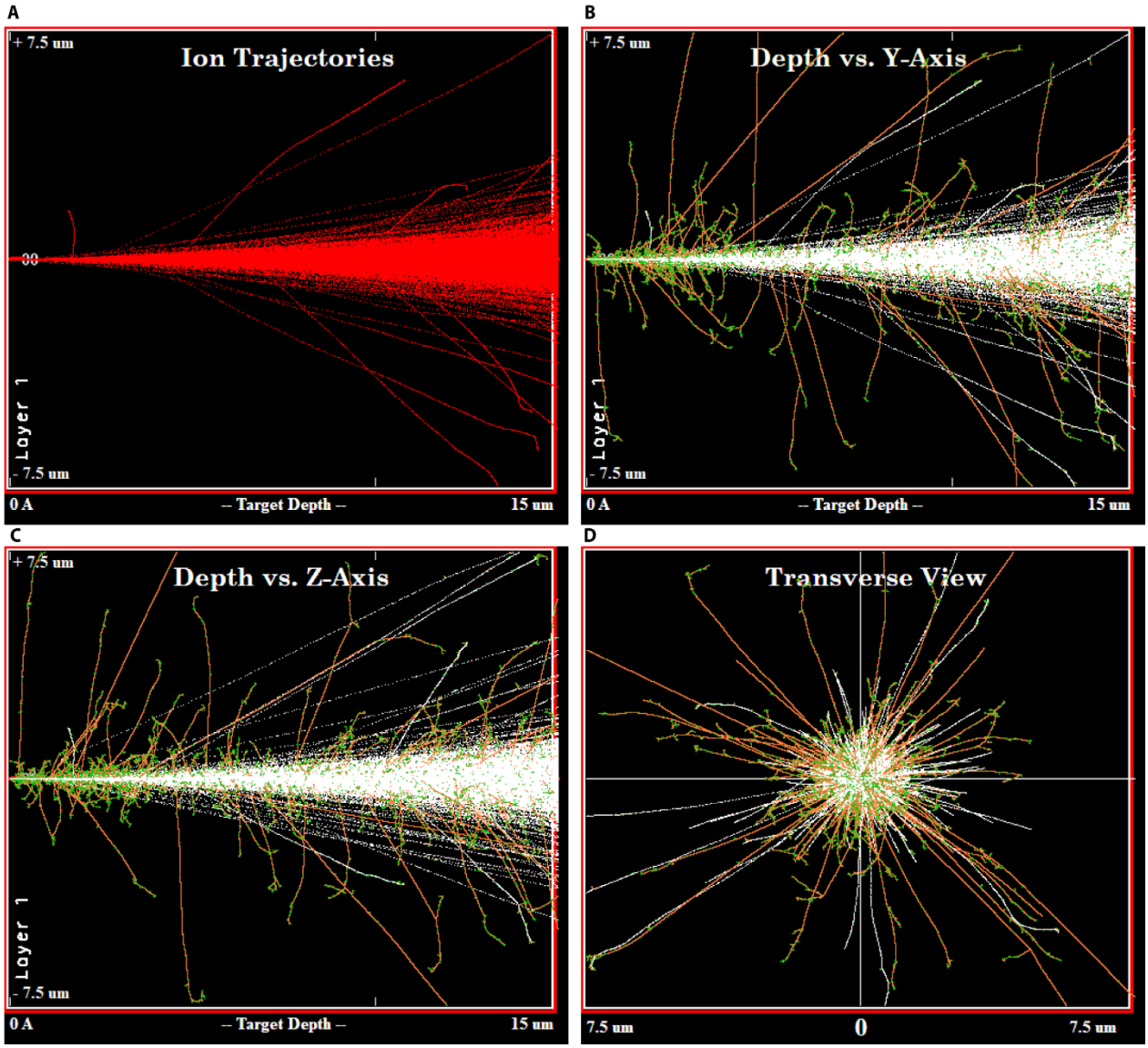

Figure.S4 The depth profile of radiation damage (in units of displacements per atom (DPA))

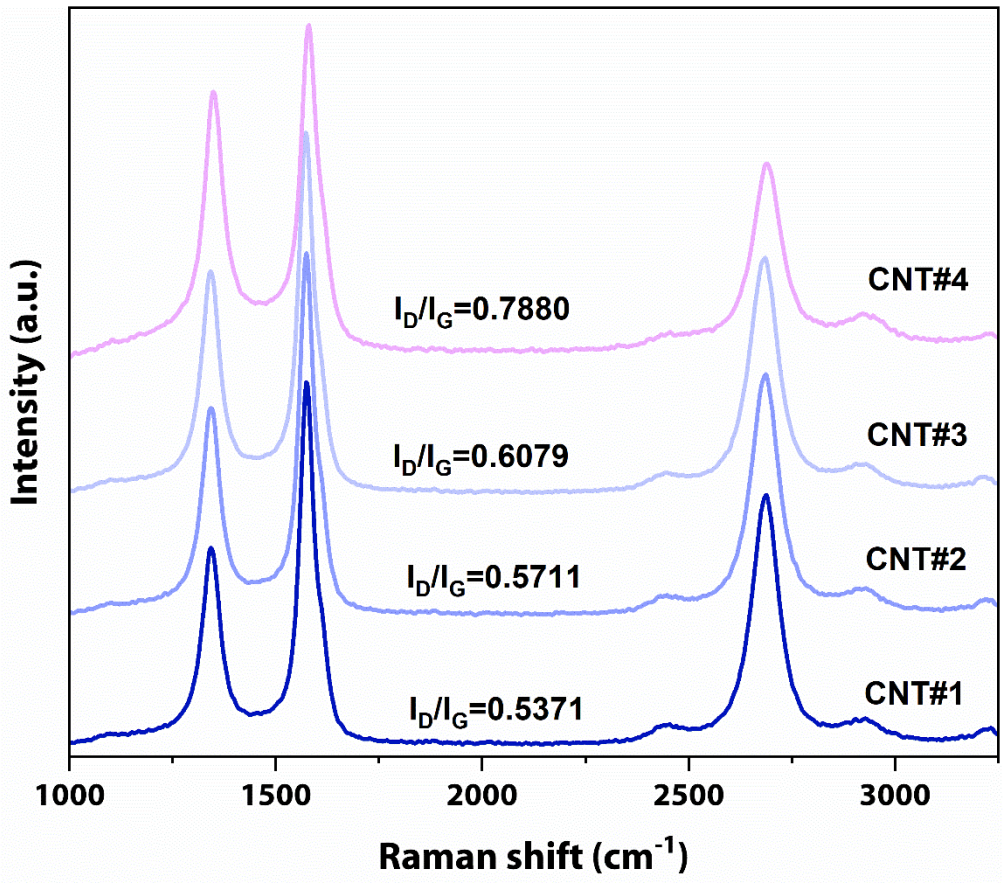

Figure.S5 Raman spectrum of pristine commercial MWCNTs and irradiated ones at ion fluences of 1×10^{13}, 1×10^{14}, 1×10^{15} ions cm^{-2}.

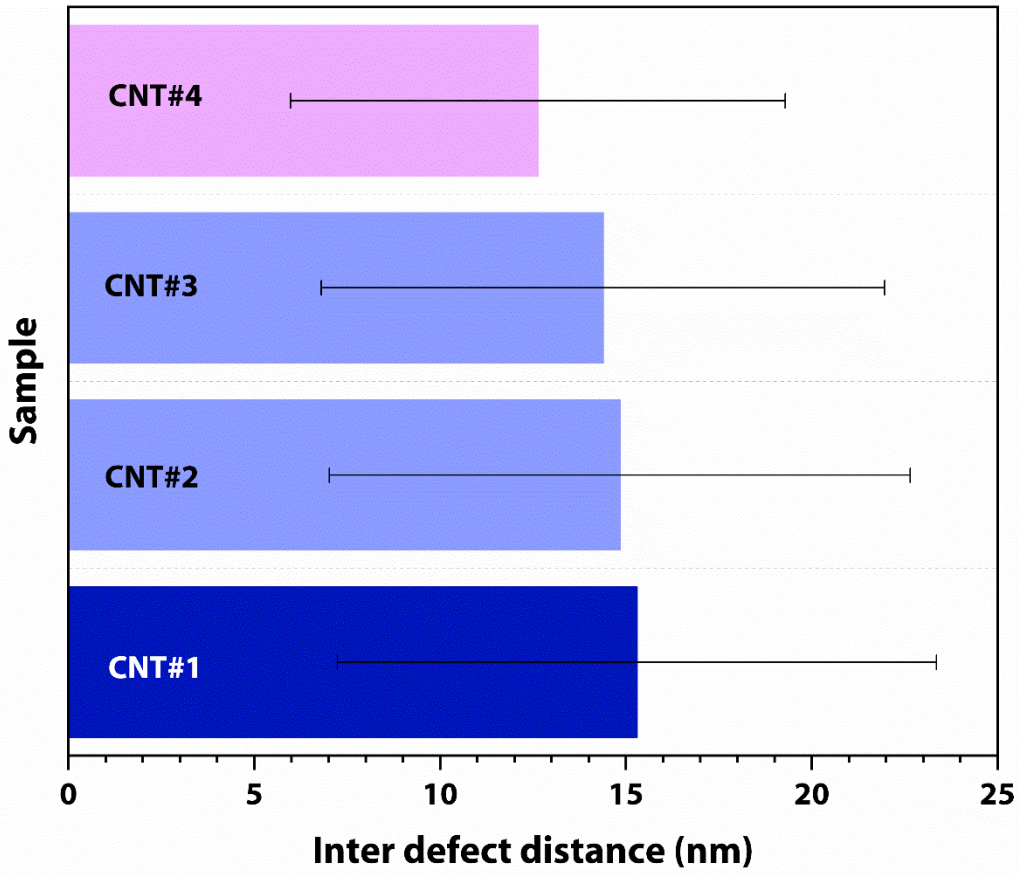

Figure.S6 Inter defect distance L_D of pristine commercial MWCNTs and irradiated ones at ion fluences of 1×10^{13}, 1×10^{14}, 1×10^{15} ions cm^{-2}.

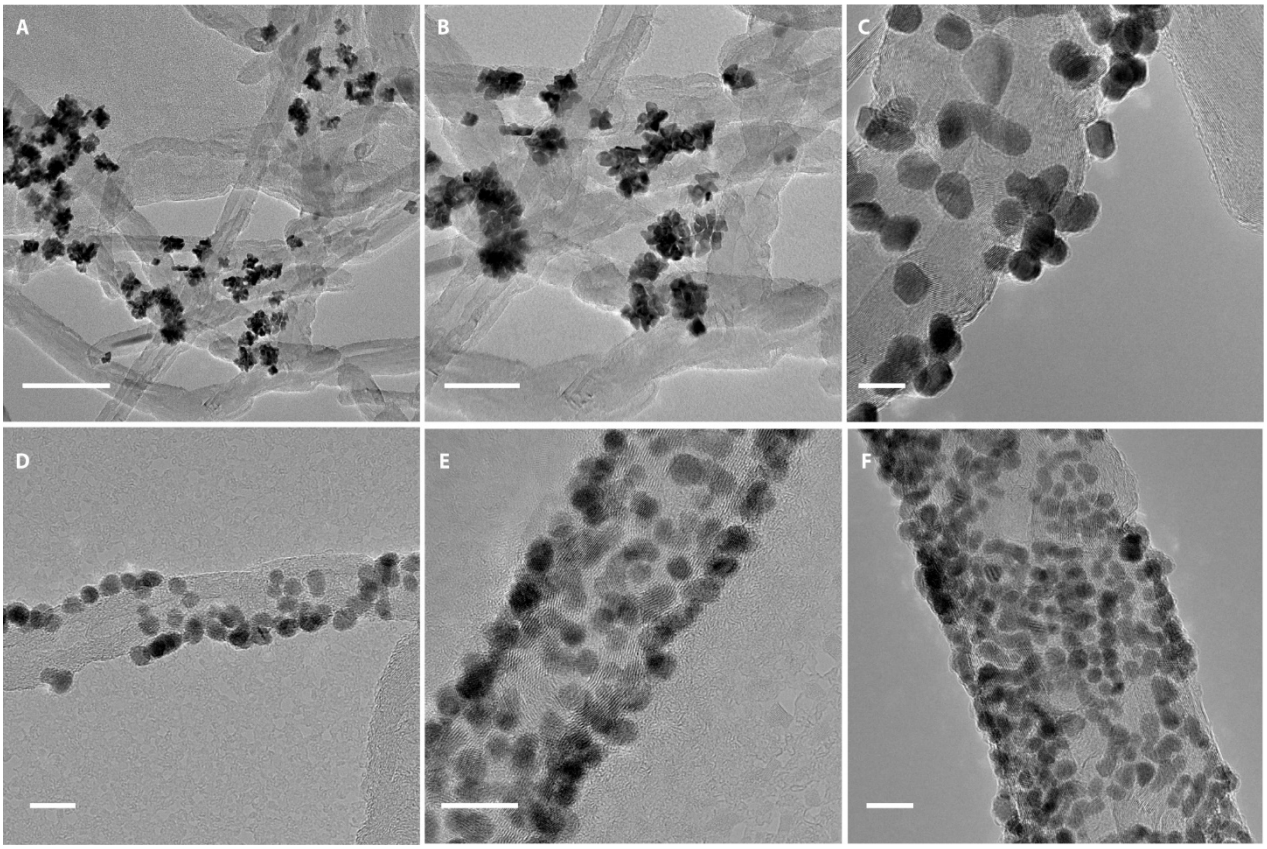

Figure.S7 Transmission Electronic Microscopy (TEM) images of platinum nanoparticles deposited on the MWCNTs irradiated at ion fluence of 1×10^{13}, 1×10^{14}, 1×10^{15} ions cm^{-2}

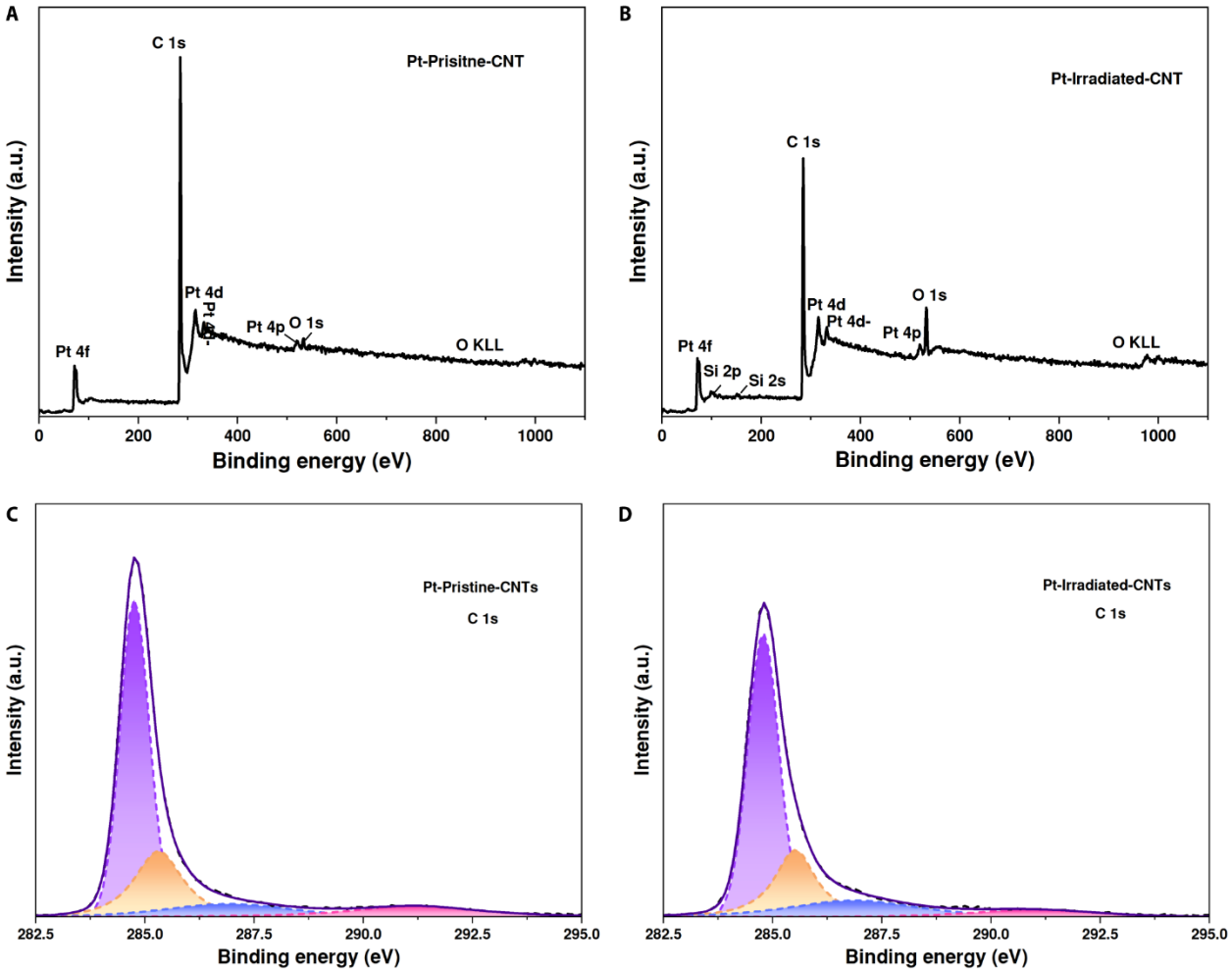

Figure.S8 X-ray Photoelectron Spectrum (XPS) of Pt-pristine-CNT, Pt-irradiated-CNT.

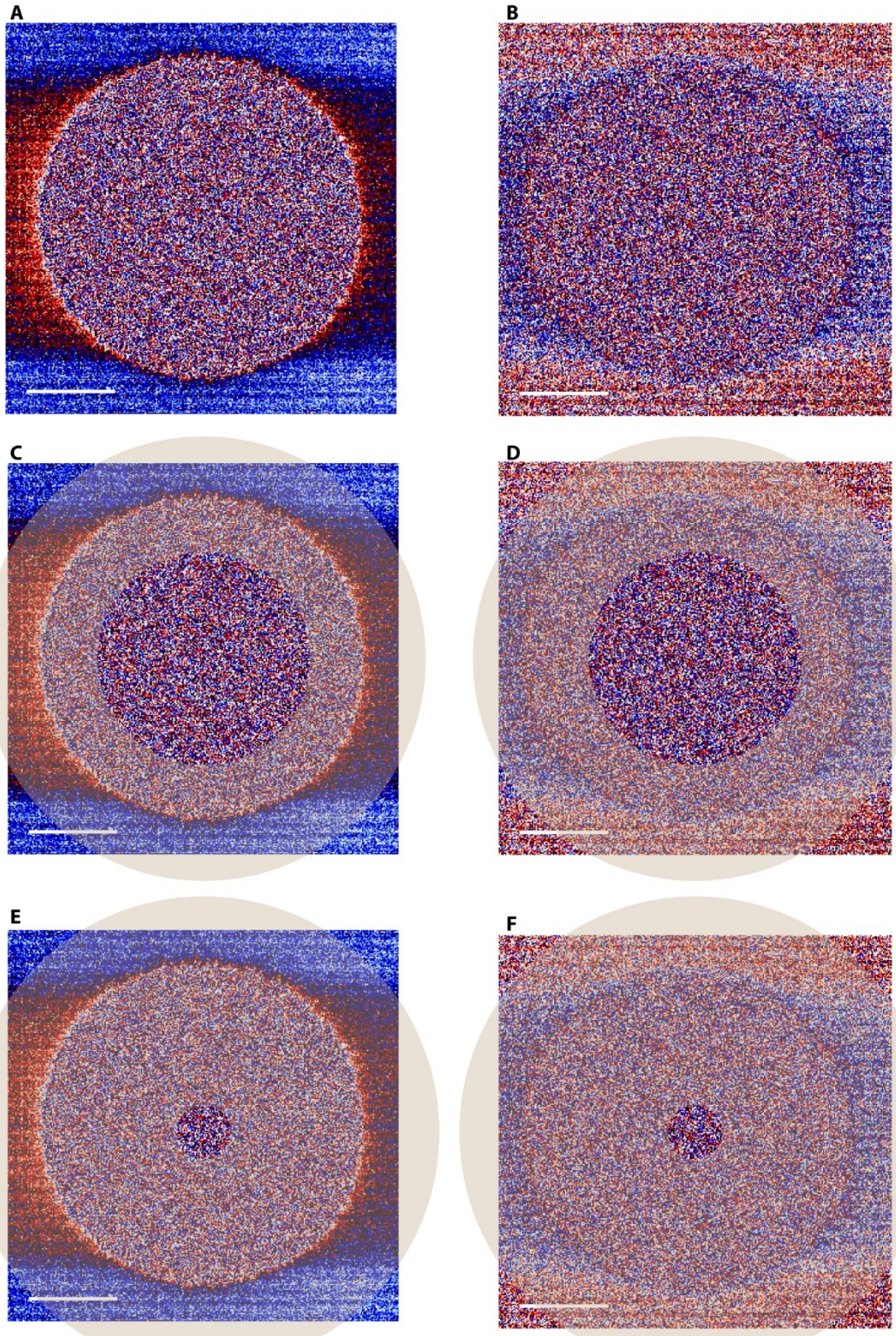

Figure.S9 The diffraction pattern of the 4D STEM datasets. A-B The diffraction pattern and mask of the Pt-irradiated-CNTs. C-D The diffraction pattern and mask of the Pt-pristine-CNTs.

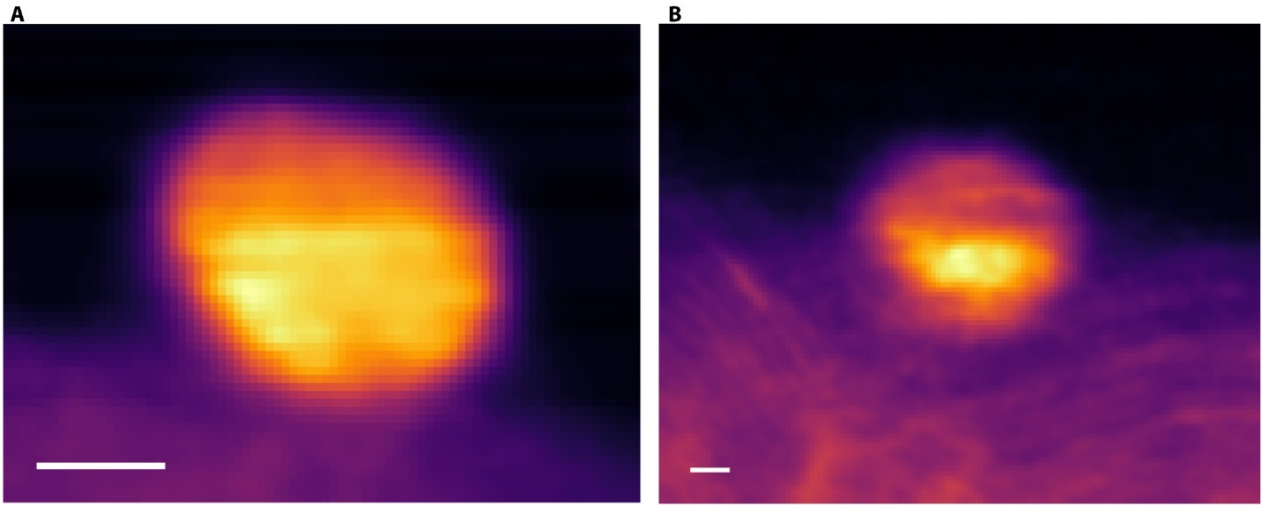

Figure.S10 Reconstructed ADF images of the Pt-irradiated-CNTs from 4D-STEM datasets.

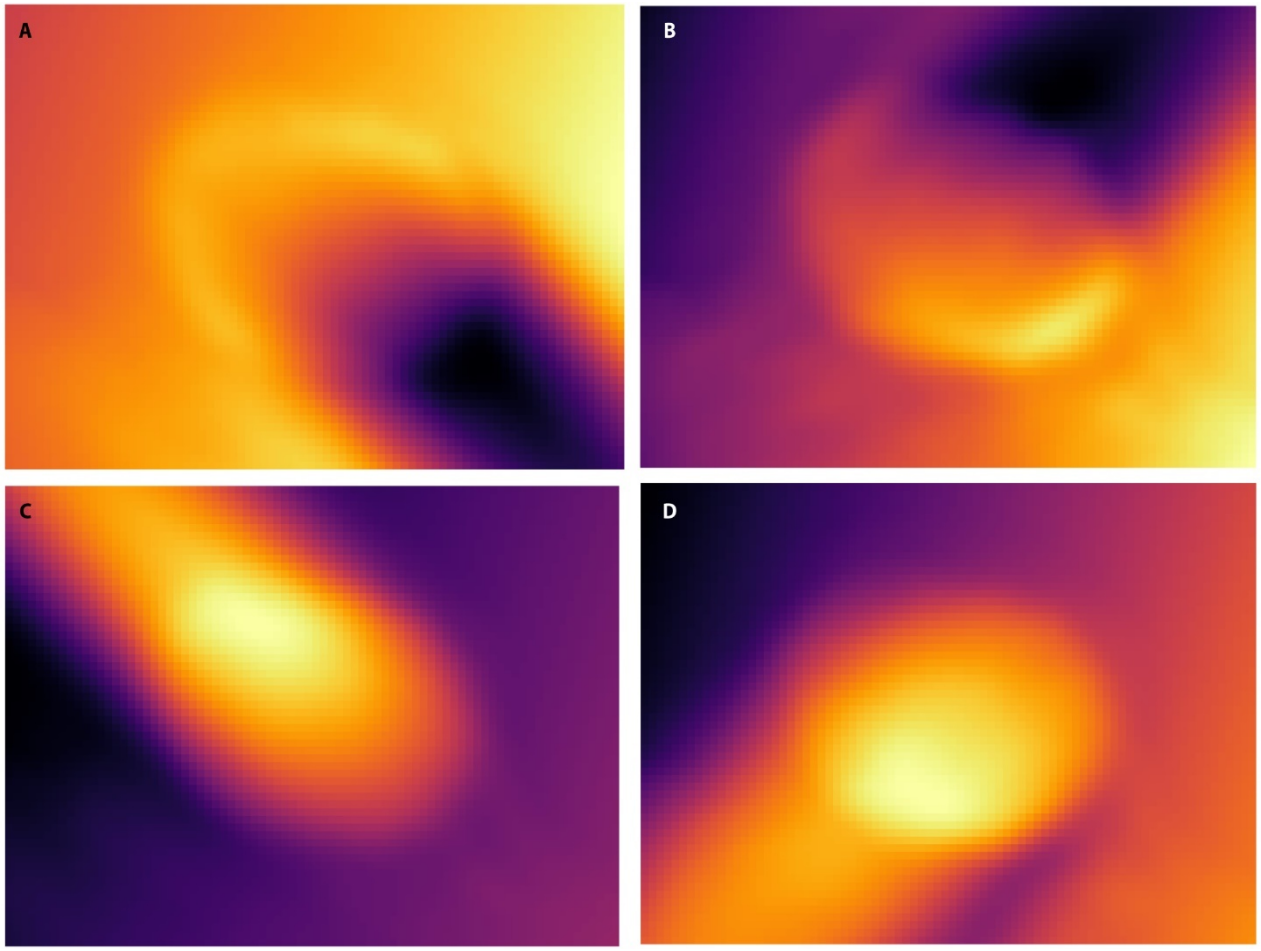

Figure.S11 Electrostatic potential distribution of the Pt-pristine-CNTs.

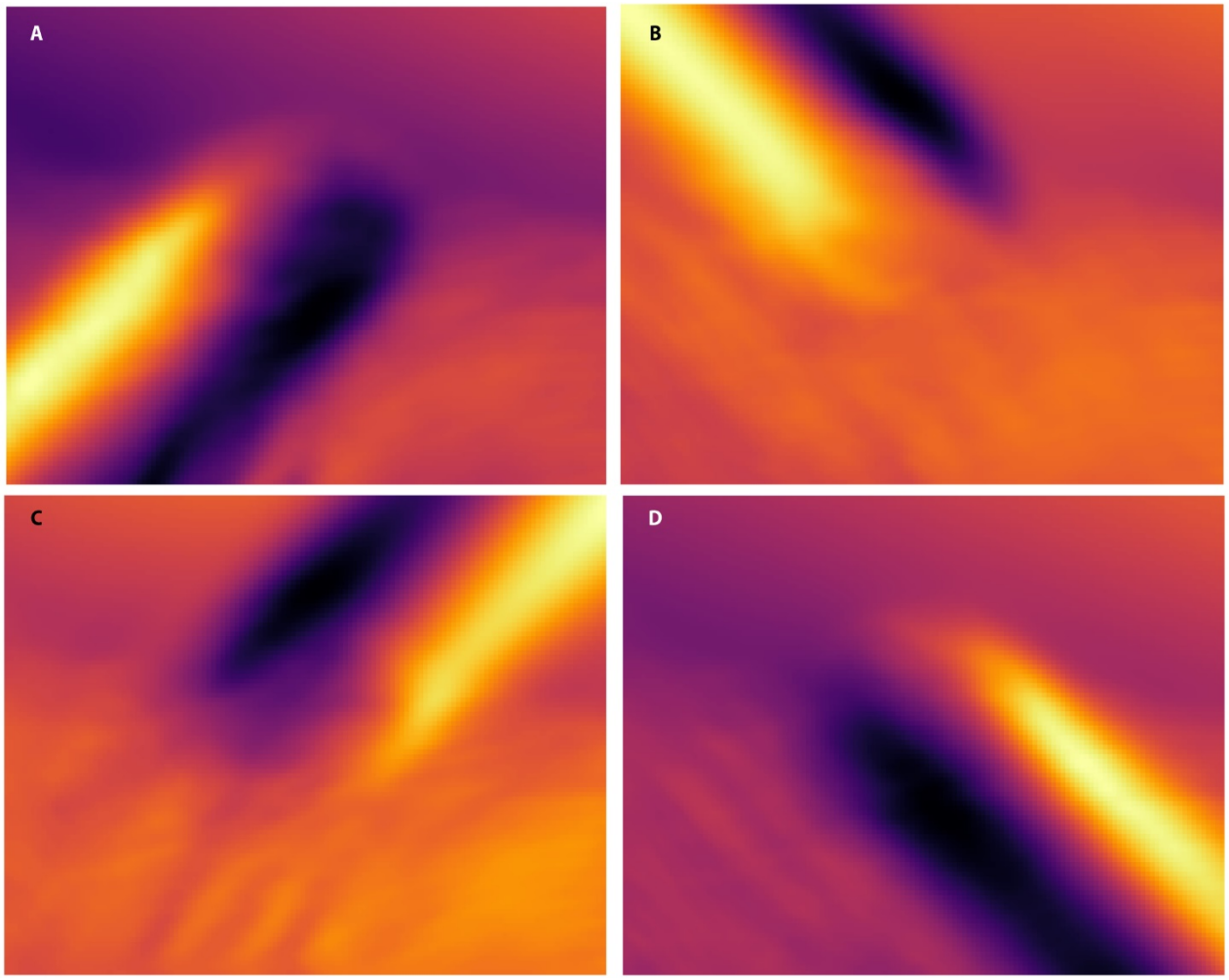

Figure.S12 Electrostatic potential distribution of the Pt-irradiated-CNTs.

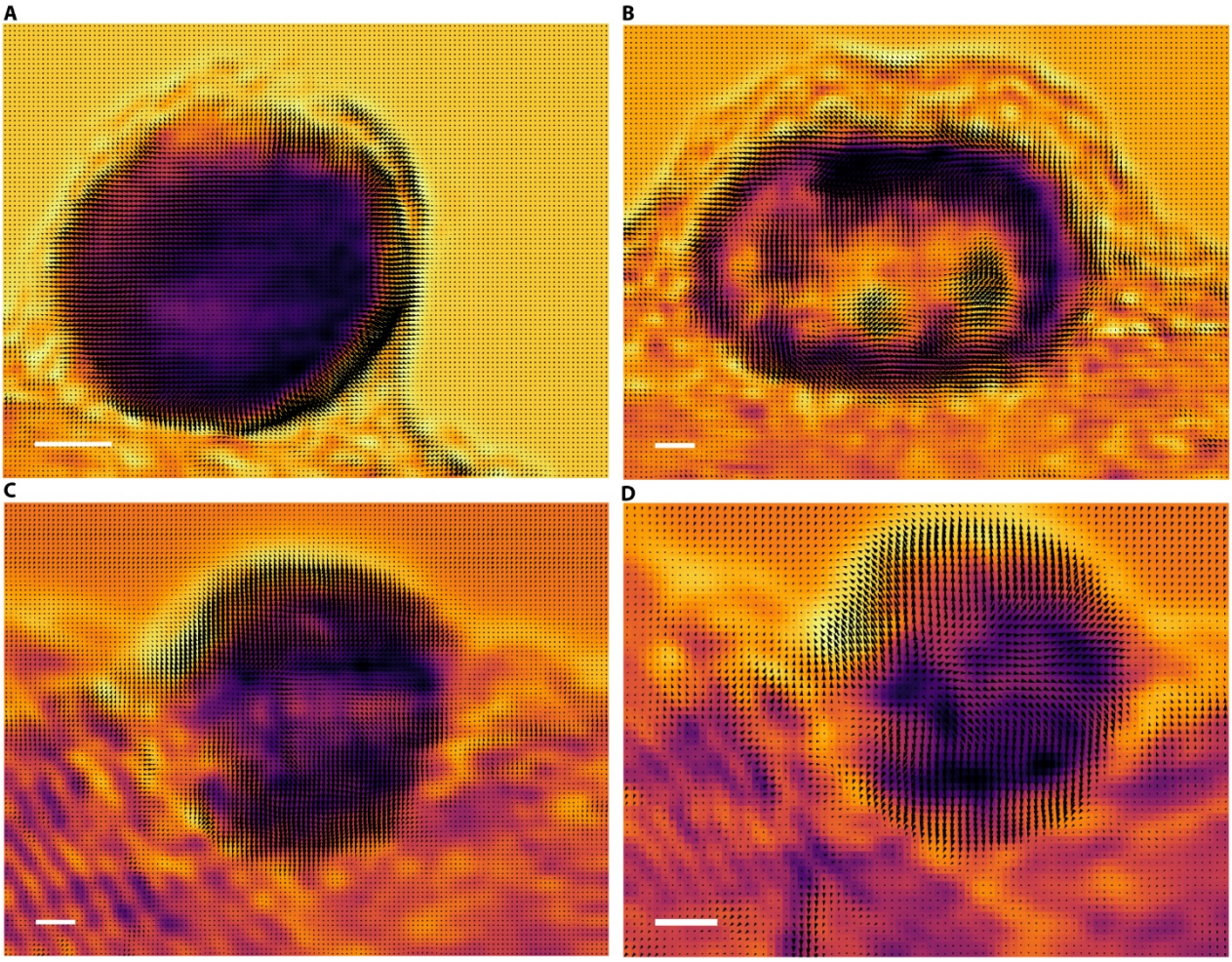

Figure.S13 Electric field distribution of (**A** and **B**) the Pt-pristine-CNTs, (**C** and **D**) the Pt-irradiated-CNTs

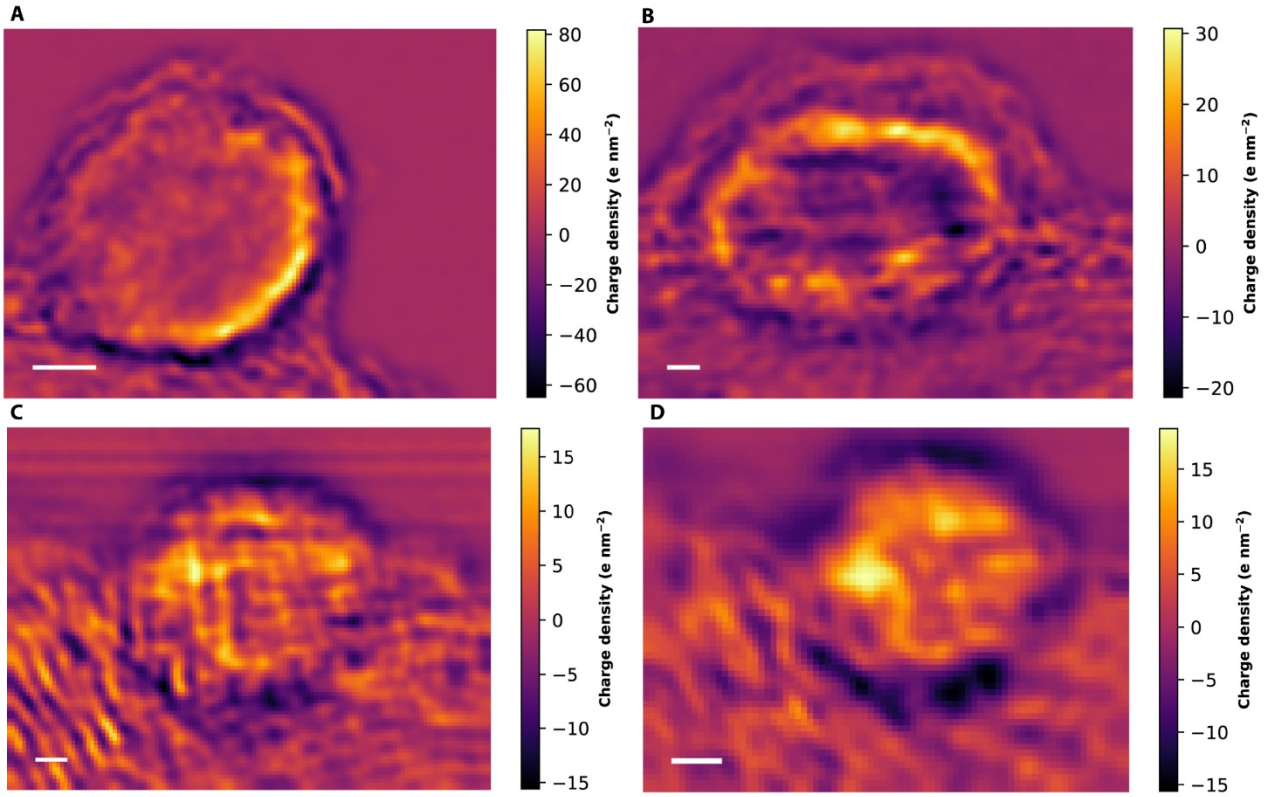

Figure.S14 Charge density mapping of (**A** and **B**) the Pt-pristine-CNTs, (**C** and **D**) the Pt-irradiated-CNTs

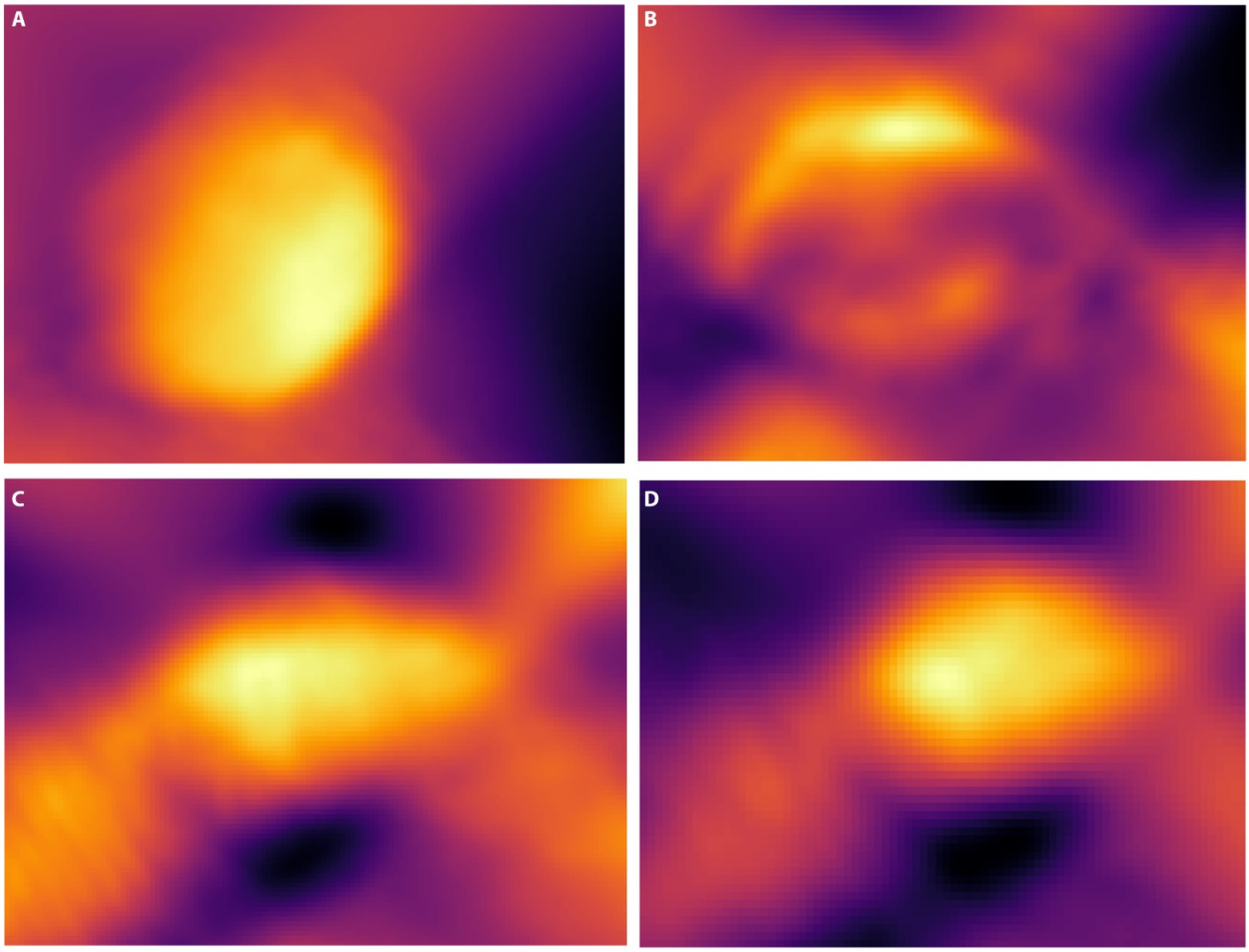

Figure.S15 Electrostatic potential distribution of (**A** and **B**) the Pt-pristine-CNTs, (**C** and **D**) the Pt-irradiated-CNTs

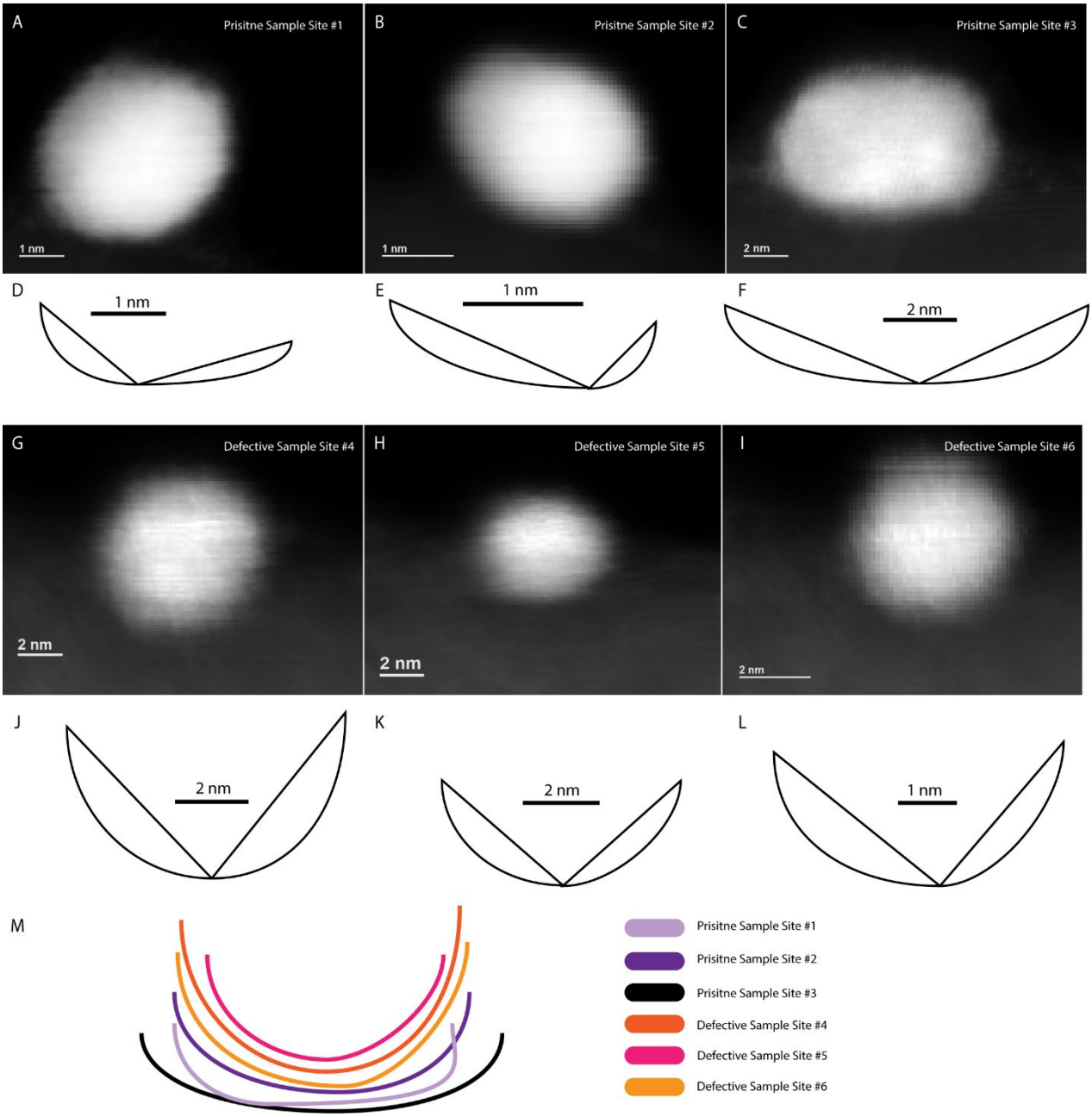

Figure.S16 The synchronized acquired HAADF images (A-C, G-I) and the fitting outer surface and the Pt-CNT interface perimeter (D-F, J-M).

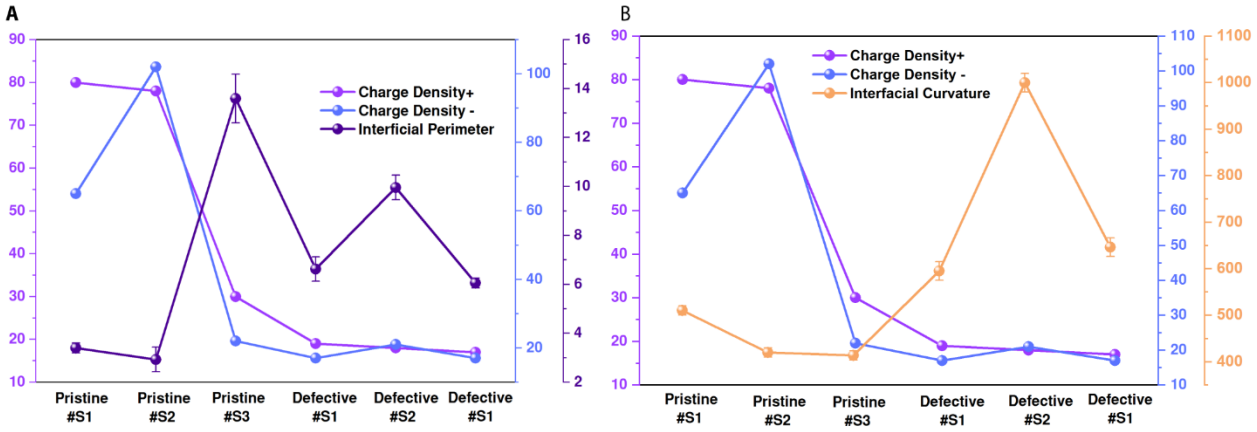

Figure.S17 The relationship curve of the charge density and the interfacial perimeter (A) and the interfacial curvature (B).

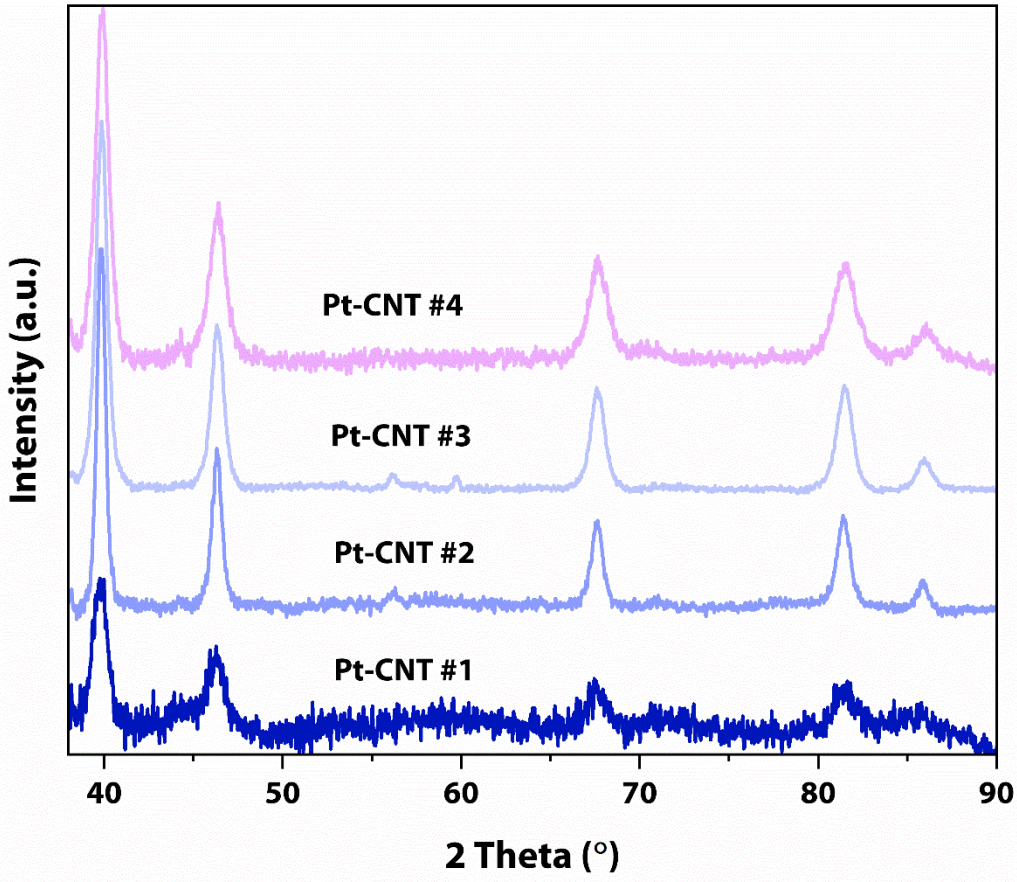

Figure.S18 X-ray diffraction spectrum of Pt-CNT #1-4

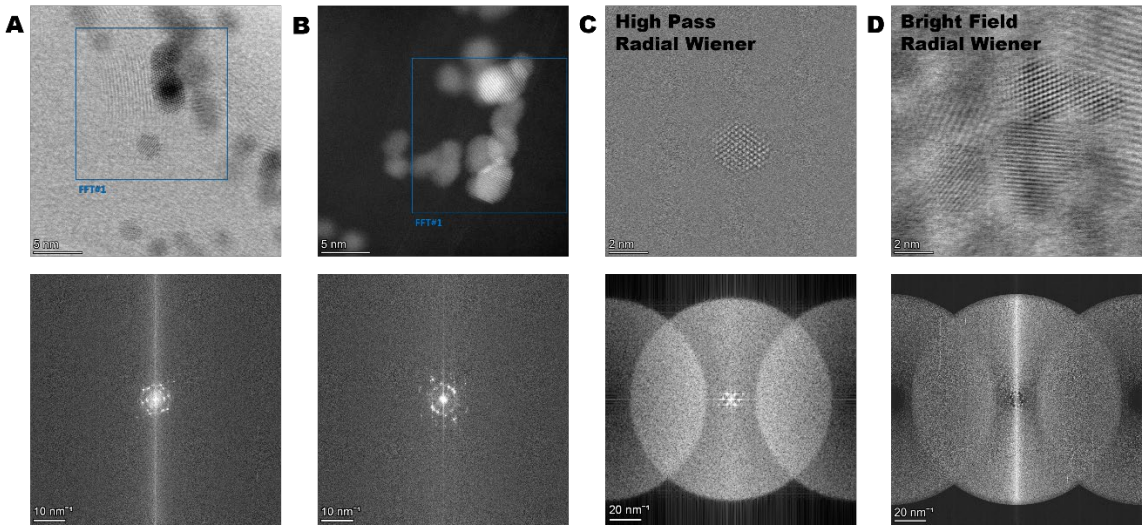

Figure.S19 Spherical aberration corrected Scanning Transmission Electron Microscope (AC-STEM) of the Pt-1E15-CNTs.

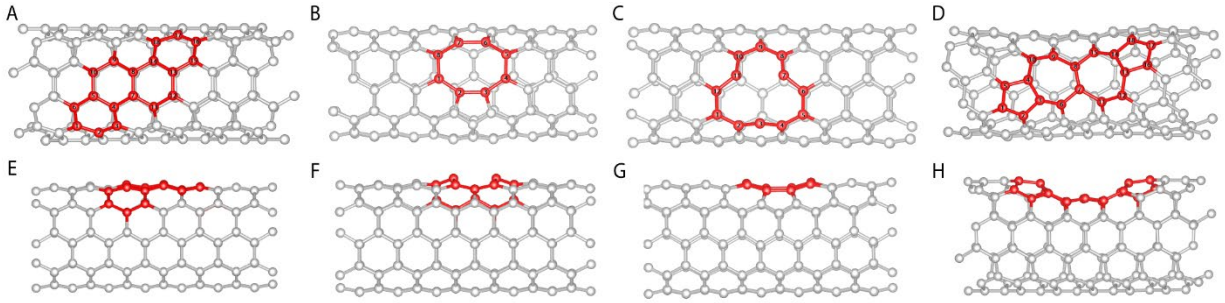

Figure.S20 Different configurations of Pristine CNT (A and E), Double vacancies CNT (B and F), Single vacancy CNT (C and G), and Stone-Wales defect CNT (D and H).

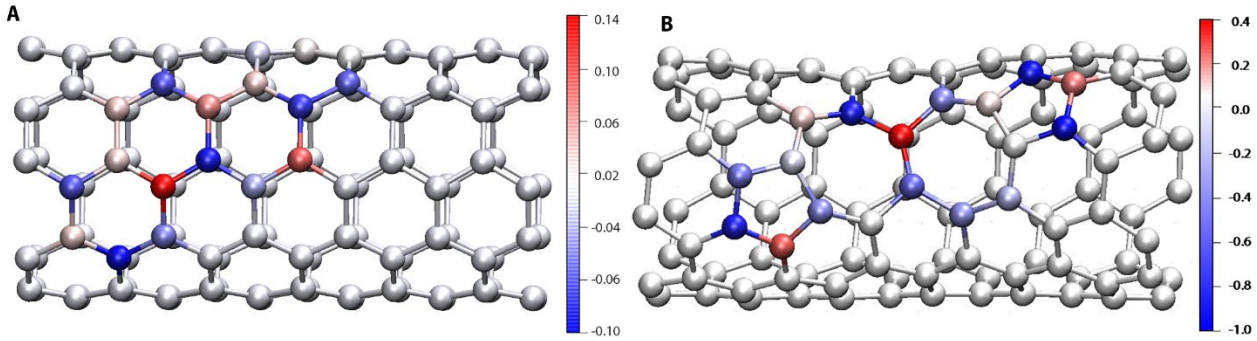

Figure.S21 Bader plots of pristine CNT (A), and CNT with Stone-Wales defect (B).

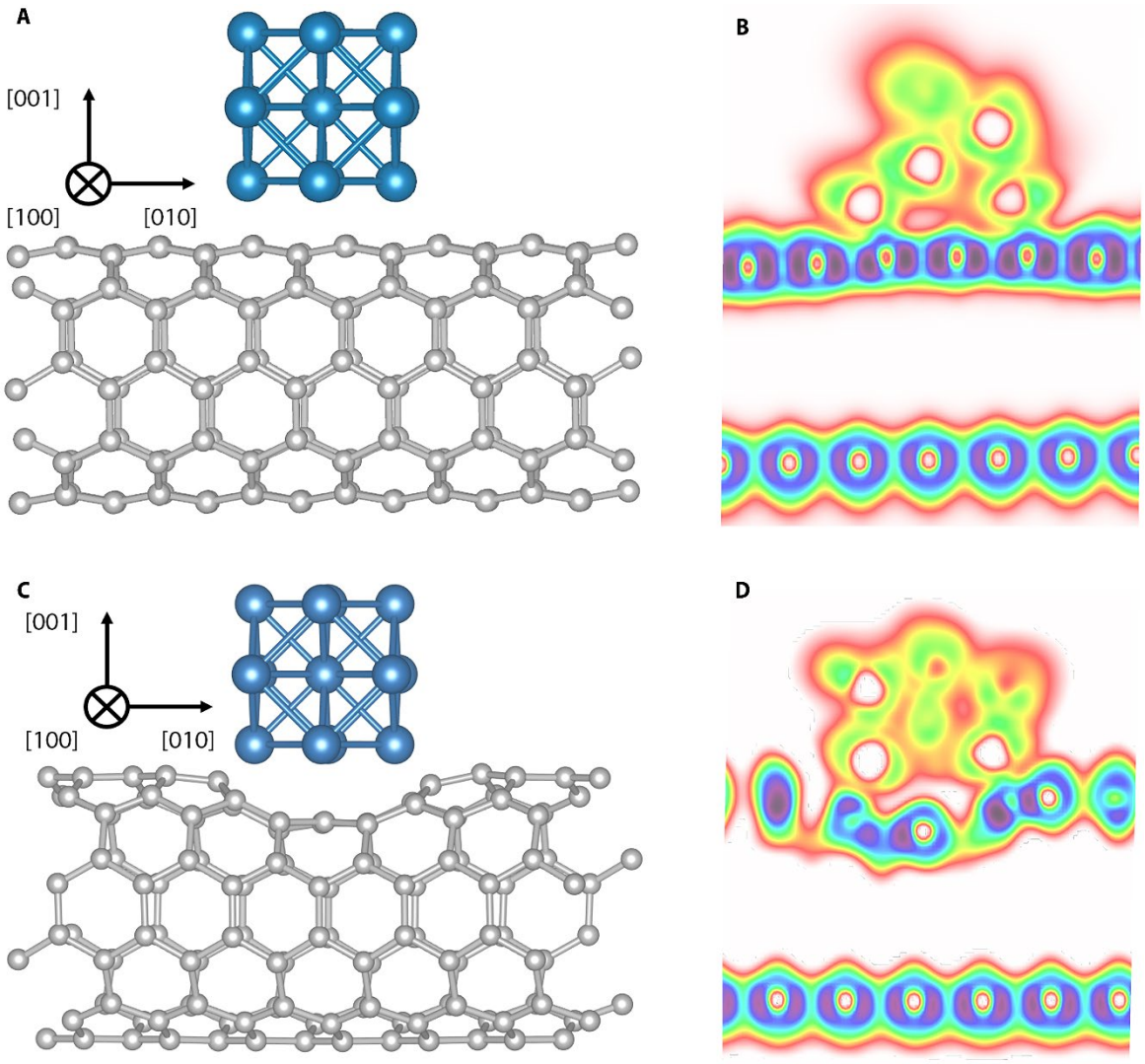

Figure.S22 Initial structures (A and C) before geometry optimization, and electron localization function (B and D) for Pt/SWCNT after geometry optimization.

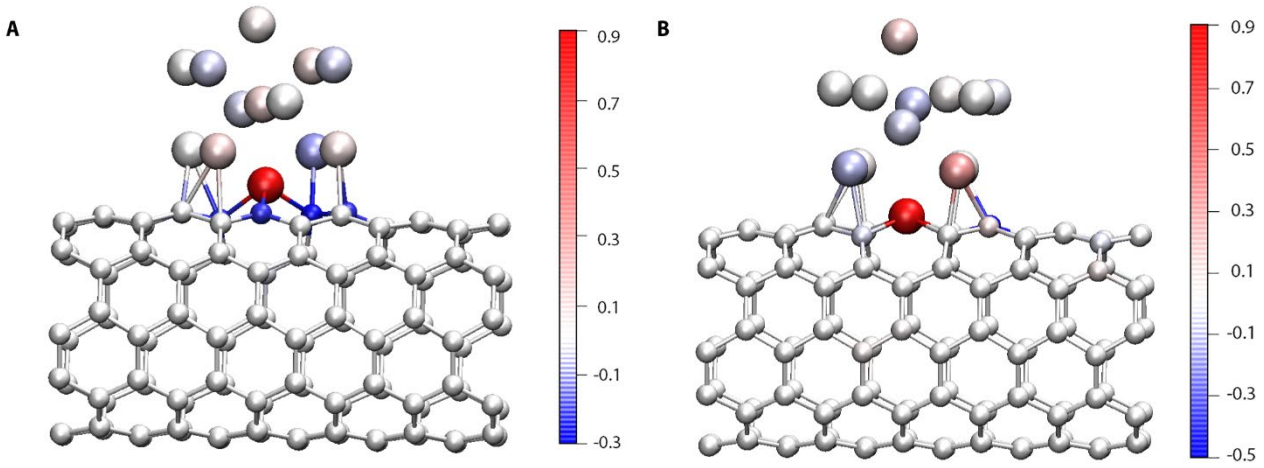

Figure.S23 Bader plots of Pt NPs loaded on SWCNT with single vacancy (A) and SWCNT with double vacancies (B).

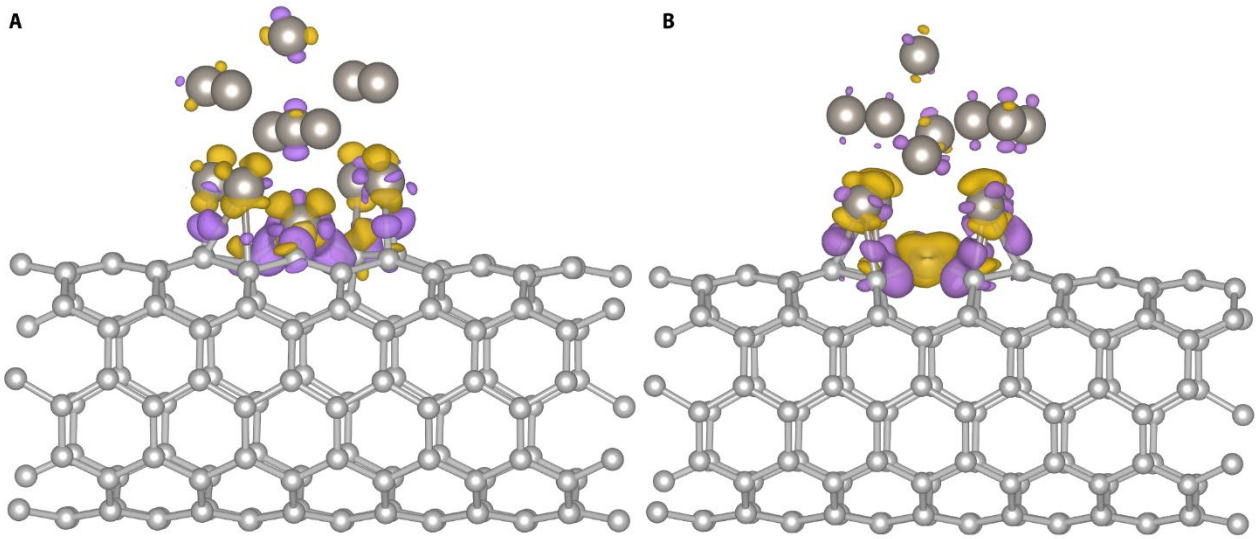

Figure.S24 (A) Charge density difference plots of Pt NPs loaded on SWCNT with single vacancy and (B) SWCNT with double vacancies (with electron reduction parts colored as yellow and electron accumulation part colored as purple).

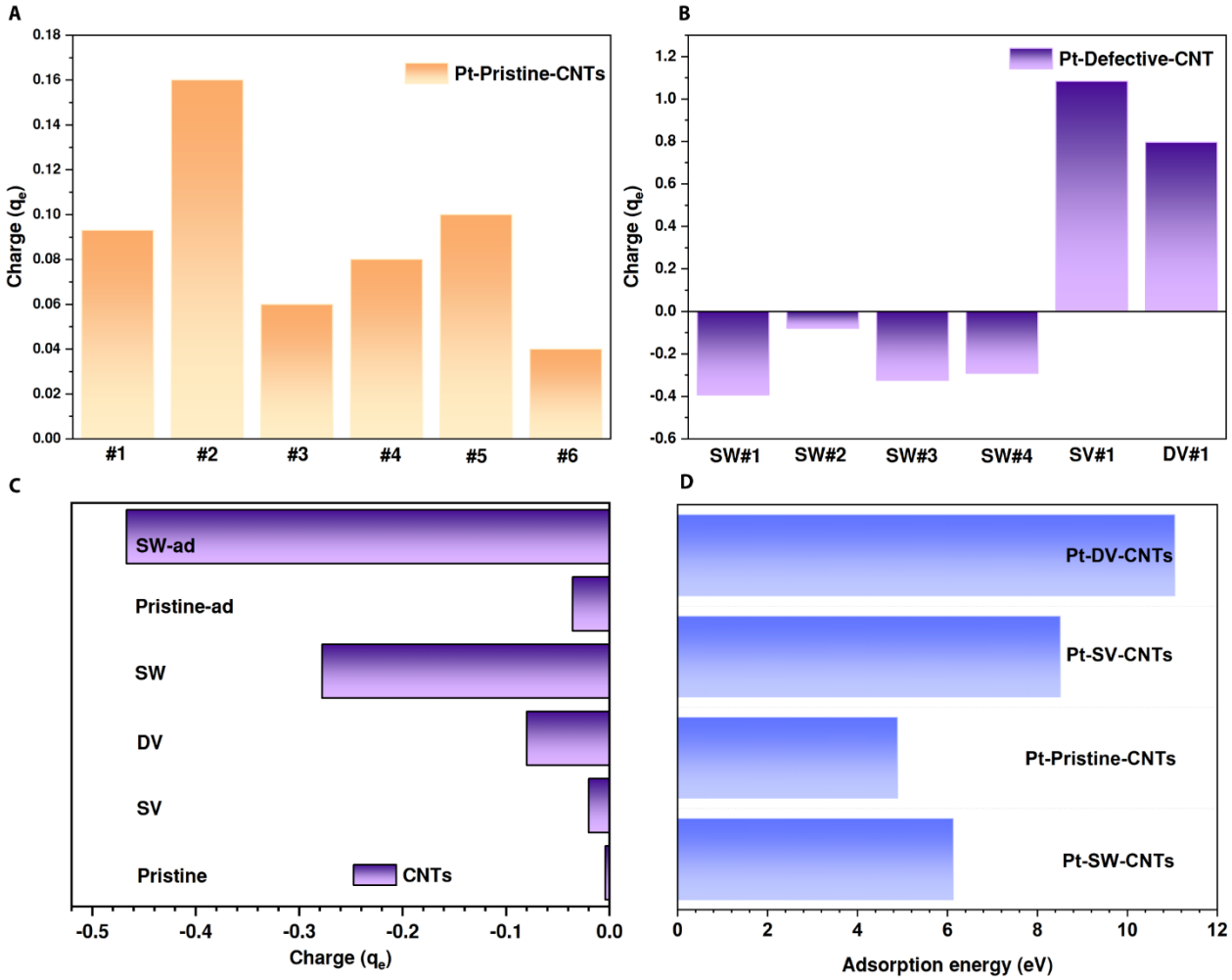

Figure.S25 Bader charge result based on different initial configuration of (A) Pt-Pristine-CNTs and (B) Pt-Defective-CNTs. (C) Bader charge of different CNTs at defective sites. (D) Adsorption energy of Pt NPs and different CNTs.

Table S1. The Raman intensity and peak ratio data

Sample Number	Irradiation Fluence /ions·cm^{-2}	I_D	I_G	I_D/I_G	L_D^2
CNT#1	0	0.50573	0.94159	0.5371	233.9213±64.978
CNT#2	1E13	0.53398	0.93499	0.5711	219.9950±61.110
CNT#3	1E14	0.56779	0.93409	0.6079	206.6773±57.410
CNT#4	1E15	0.65835	0.83547	0.7880	159.4405±44.289

Density of point like defects in Graphene/CNTs:

$$L_D^2(nm^2) = (1.8 \pm 0.5) \times 10^{-9} \cdot \lambda_{laser}^4 \left(\frac{I_D}{I_G}\right)^{-1} \quad (9)$$

Where λ_{laser} refers to the wavelength of the Raman laser, here the laser wavelength is 514 nm.

Table S2. The calculated perimeter and average curvature of Pt-pristine-CNTs and Pt-irradiated-CNTs at sites #1-3

Sample Number	**#Prisitine S1**	**#Prisitine S2**	**#Prisitine S3**
Size	4.461±0.2 nm	2.92±0.2 nm	9.914±0.2 nm
Perimeter	3.395±0.2 nm	2.93±0.5 nm	13.595±1 nm
Average curvature	510.06±10 μm^{-1}	419.664±10 μm^{-1}	413.626±10 μm^{-1}
Sample Number	**#Irradiated S1**	**#Irradiated S2**	**#Irradiated S3**
Size	4±0.2 nm	6.602±0.2 nm	3.822±0.5 nm
Perimeter	6.232±0.5 nm	9.96±0.5 nm	6.056±0.2 nm
Average curvature	594.87±20 μm^{-1}	999.836±20 μm^{-1}	646.395±20 μm^{-1}

Table S3. Bader charge by DFT calculations with no defects.

	Case 1	**Case 2**	**Case 3**	**Case 4**	**Case 5**
Charge	+0.16	+0.06	+0.08	+0.1	+0.04
Direction	Pt to CNT	Pt to CNT	Pt to CNT	Pt to CNT	Pt to CNT

Table S4. Bader charge by DFT calculations with defects.

	5775-CNT	SV-CNT (embedded)	DV-CNT (embedded)
Charge	-0.39	1.1	0.8
Charge transfer Direction	CNT to Pt	Pt to CNT	Pt to CNT

254 **Table S5.** Adsorption energy for different Pt-CNT models.

	Pt-Pristine-CNT	Pt-5775-CNT	Pt-SV-CNT	Pt-DV-CNT
Adsorption energy	-6.127	-4.887	-6.193	-6.135

255

256 **Table S6.** Bader charge of CNTs in defect area after adsorption.

SWCNT model system	Charges on CNT surface
Pristine	-0.0357
Stone-Wales defects	-0.462

257

258

Table S7. Bader charge of interface between of Pt NPs and CNTs.

Pt-CNT model system	Pt-CNT-interface (C atom)	Pt-CNT-interface (Pt atom)	Pt-CNT (Pt NP total)
Pristine	-0.655	0.234	0.093
Stone-Wales defects	0.178	-1.065	-0.393

Table S8. Bader charge of different atoms in defect area.

Pt-CNT model system	Pt1	Pt2	Pt3	C1	C2	C3	C4	C5	C6
Stone-Wales defects	-0.027	0.043	-1.081	0.102	-0.185	0.090	-0.002	0.166	0.007

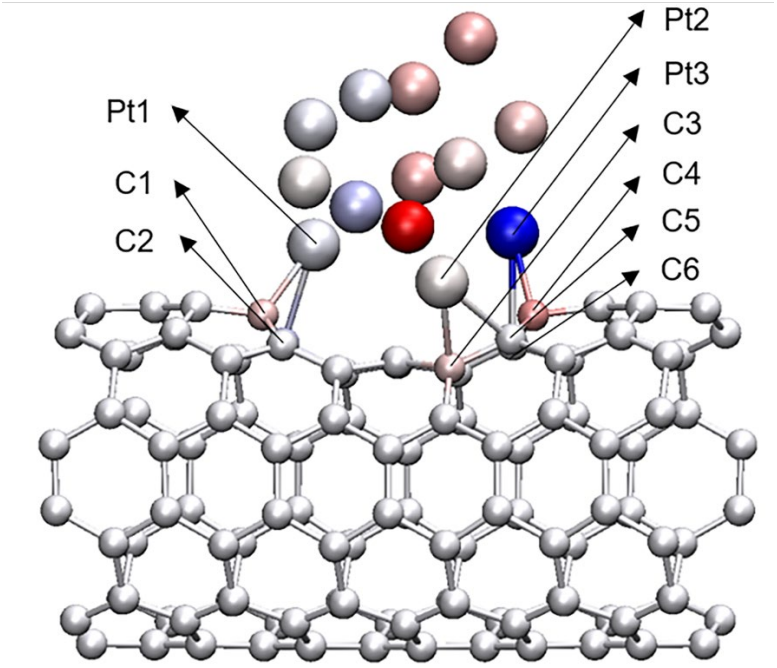

Pt-CNT model system	Pt1	Pt2	Pt3	Pt4	C1	C2	C3	C4	C5	C6	C7	C8
Pristine	0.300	-0.299	0.203	0.030	-0.442	-0.062	0.513	-0.798	0.829	-0.491	-0.569	0.365

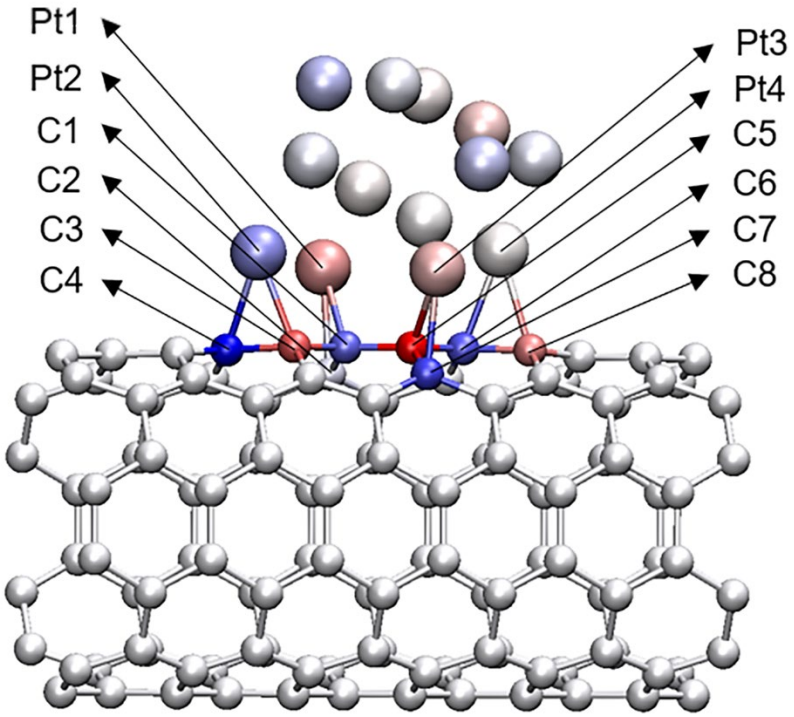

265